Received: 23 October 2017 | Revised: 10 May 2018 | Accepted: 16 May 2018

DOI: 10.1002/pip.3037

RESEARCH ARTICLE

WILEY PROGRESS IN PHOTOVOLTAICS

Perovskite/c-Si tandem solar cells with realistic inverted architecture: Achieving high efficiency by optical optimization

Lixiang Ba[1] | Hong Liu[1] | Wenzhong Shen[1,2]

[1] Institute of Solar Energy and Key Laboratory of Artificial Structures and Quantum Control (Ministry of Education), School of Physics and Astronomy, Shanghai Jiao Tong University, Shanghai 200240, People's Republic of China

[2] Collaborative Innovation Center of Advanced Microstructures, Nanjing 210093, People's Republic of China

Correspondence
Hong Liu, Wenzhong Shen, Institute of Solar Energy and Key Laboratory of Artificial Structures and Quantum Control (Ministry of Education), School of Physics and Astronomy, Shanghai Jiao Tong University, Shanghai 200240, People's Republic of China.
Email: liuhong@sjtu.edu.cn; wzshen@sjtu.edu.cn

Funding information
Natural Science Foundation of China, Grant/Award Numbers: 61234005, 11674225 and 11474201

Abstract

Many theoretical analyses for perovskite/c-Si monolithic tandem solar cells (TSCs) have shown optical optimization and high efficiency limits, but they use many idealized assumptions and draw some unpractical conclusions for experiments. In this work, we have introduced a composite method combining the finite difference time domain and light path analysis for the first time. By using this method, we have systematically calculated perovskite/c-Si monolithic TSCs with inverted architecture based on realistic solar cell parameters. Theoretical results have demonstrated very good match of the experimental external quantum efficiencies of both subcells. More importantly, from optical and electrical point of view, we have analyzed current losses of such TSCs and proposed detailed optimization for achieving high efficiency. Finally, we have presented improved configuration of perovskite/c-Si monolithic TSCs with addition of pyramids structure in front surface, which can effectively increase the tandem cell efficiency to 29.05%. This work can be served as a practical guidance for the realization of high-efficient perovskite/c-Si monolithic TSCs.

KEYWORDS

FDTD, inverted configuration, light path analysis, optical and electrical optimization, perovskite/c-Si monolithic TSCs

1 | INTRODUCTION

Crystalline silicon (c-Si) solar cells occupy an important position in photovoltaic market (over 90%) because of its low cost, high efficiency, and mature industrialization. The world record efficiency of 26.6% reported by Yoshikawa et al[1] is extremely close to the Shockley-Queisser efficiency limit, so further improvement becomes very difficult. In recent years, many groups have studied perovskite because of its high absorption coefficient, sharp absorption edge, and tunable bandgaps. The efficiencies have increased from 3.8%[2] in 2009 to 22.1%[3] in 2017, but further enhancement also faces difficulties. c-Si and perovskite have bandgaps of 1.1 eV and 1.5 to 2.3 eV, respectively, which are suitable for spectrum matching so as to break the limit for even higher efficiencies. Some theoretical calculations have assessed efficiency limits of perovskite/c-Si tandem solar cells (TSCs) with >30%.[4-7] Tandem solar cells can be fabricated mainly with 2 different configurations: mechanically stacked (4-terminal) or monolithically integrated (2-terminal) tandems. Compared with 4-terminal configuration,[8-11] 2-terminal configuration has less complexity and better feasibility in application fields.

To date, many experimental works[12-16] have been contributed to reduce current losses and enhance the best matched short-circuit current density in the perovskite/c-Si monolithic TSCs. The first experimental record was 13.7% by Mailoa et al[12] in 2015, and soon increased to 23.6% by Bush et al[14] in 2017 with reduction of parasitic absorption and recombination in different layers and interfaces by using more suitable materials and fabricating thinner carrier transport layers. Nevertheless, even the best optimized record has not yet exceeded that for pure silicon solar cells[1] and far below its theoretical prediction.[5] Therefore, more realistic approach for the mechanism study would be necessary to understand such difference and search for any possibilities to change that. Previously, many theoretical works[4-7,17,18] have thoroughly elucidated light trapping in top cell and optimized front surface textures such as pyramids and inverted

nanopyramids by using the finite difference time domain (FDTD) or transfer matrix method (TMM). Shi et al[5] reported perovskite/c-Si monolithic TSCs with inverted nanopyramids and achieved current matching by adding a well-designed intermediate contact layer as reflector for short wavelengths. Santbergen et al[4] simulated monolithic perovskite/c-Si tandem devices with different textured configurations and achieved the best matched short-circuit current density by tuning interlayer/burial layer refractive index. However, these results directly ignored parasitic absorption of some layers,[4] used experimentally unreasonable thickness of perovskite layer,[6] or overlooked some electrical properties.[5] More detailed theoretical calculation is probably necessary to include those factors, which could have played important role and cannot be simply approximated.

In this study, we have introduced a composite method combining FDTD and light path analysis together for the TSCs or devices for the first time. The combination, in addition with effective long wavelength modification, can hopefully resolve the problems induced by the vast scale difference between grid cells and devices using either FDTD or analytical calculation alone. Comparing with other methods such as TMM, FDTD is easier to solve problems and get visual results in time domain.[19,20] We have thoroughly calculated perovskite/c-Si monolithic TSCs absolutely relying on reliable experimental thicknesses and materials. Simulated results have shown quite good match with the latest and best experimental report of external quantum efficiencies (EQE) of both subcells.[14] We have carried out detailed optimization for achieving high efficiency in perovskite/c-Si monolithic TSCs, including the cell configuration, thickness and bandgap of perovskite layers, and current loss in different layers. It is found that there are significant current losses in surface reflection of TSCs and parasitic absorption of indium tin oxide (ITO) layer, which could be the main ways for the further improvement in experiments. Finally, we have further suggested that addition of pyramids structure in front surface can effectively increase the TSC efficiency of 23.6% to 29.05%, which has given light to the experimental research of real applicable high-performance perovskite/c-Si tandem cells. This work could hopefully facilitate a more detailed understanding of the optoelectronic mechanisms of perovskite/c-Si monolithic TSCs and more significant improvement of their performance in application.

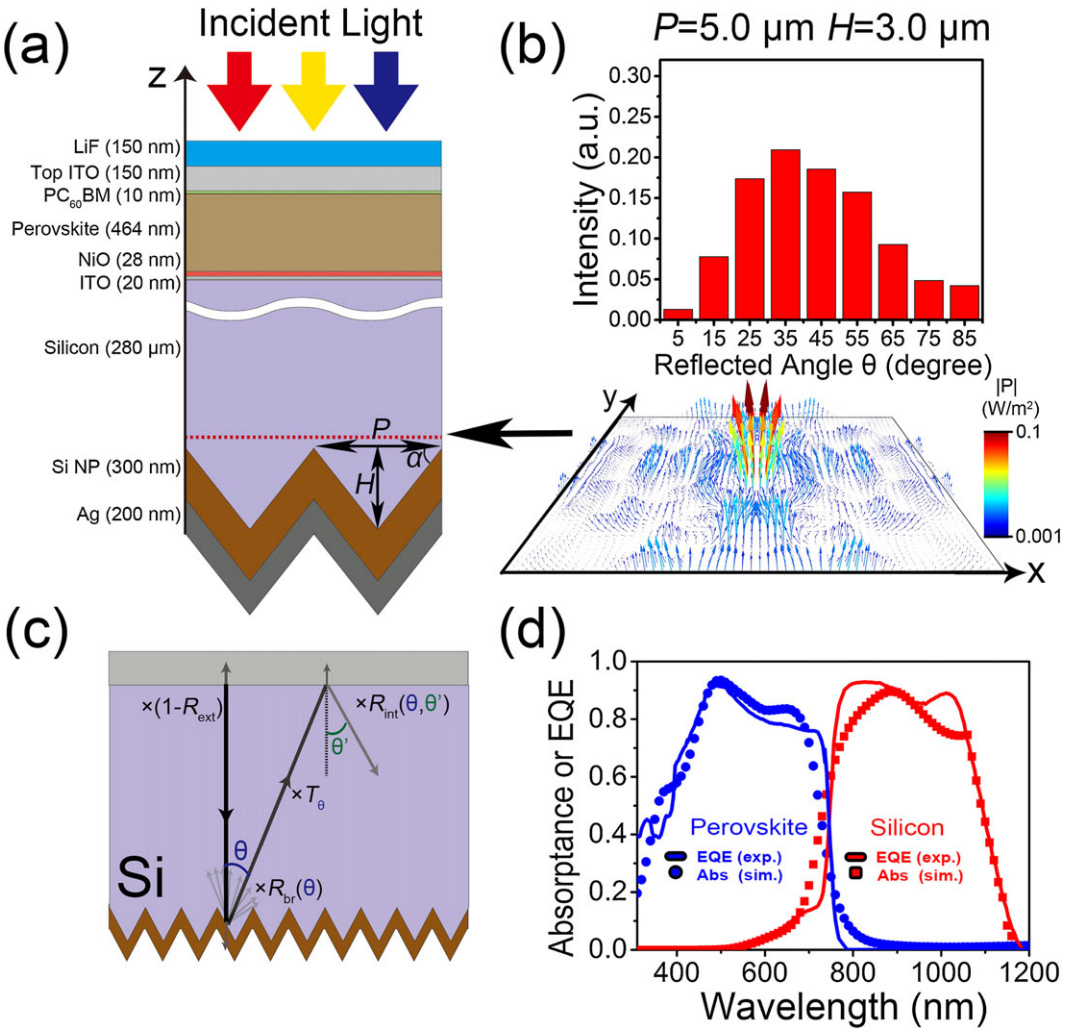

FIGURE 1 A, Schematic drawing of perovskite/c-Si monolithic TSCs with flat front surface and pyramid-textured rear surface. The parameters α, P, and H denote the pyramid base angle, period, and height, respectively. B, Angular distribution and the 3-dimensional vector distribution for λ = 1100 nm, P = 5.0 μm, and H = 3.0 μm. C, Illustration of the absorption process of the silicon layer. D, Simulated absorptance of both subcells in perovskite/c-Si monolithic TSCs (the dotted lines) and the measured EQE of both subcells (the curves) [Colour figure can be viewed at wileyonlinelibrary.com]

2 | METHODS AND VALIDATION

The simulated monolithic TSCs considered here are the current world record perovskite/c-Si TSCs with an efficiency of 23.6%.[14] The solar cell, of which a schematic drawing is shown in Figure 1A, consists of a 150-nm-thick lithium fluoride (LiF) antireflective layer, a 150-nm-thick transparent conductive oxide layer of top ITO with a carrier concentration of 2.0×10^{20} cm^{-3}, a 10-nm-thick electron transport layer of $PC_{60}BM$, a 464-nm-thick perovskite layer ($Cs_{0.17}FA_{0.83}Pb(Br_{0.17}I_{0.83})_3$, with a bandgap of 1.63 eV), a 28-nm-thick hole transport layer of NiO, a 20-nm-thick transparent conductive oxide layer of ITO with a carrier concentration of 5.0×10^{20} cm^{-3}, and a 280-μm-thick single-side-textured (SST) c-Si/amorphous silicon heterojunction solar cell. This silicon solar cell includes a polished front surface, a micron-sized pyramid-textured rear surface (ca. 5.0 μm), a 300-nm-thick silicon nanoparticle (NP) layer (with a refractive index of 1.4), and a 200-nm-thick silver back layer. Other amorphous silicon thin film layers whose thicknesses were less than 10 nm were eliminated from our optical model. The thicknesses of all layers were all acquired from Bush et al,14 and the refractive indexes and extinction coefficients of all materials were obtained from the recent literatures.[21-25] As a highly insulating layer, LiF had negligible influence on the total absorption because of the extremely low extinction coefficients and high work function.[21] Therefore, we fixed the thickness (150 nm), refractive index (1.39), and extinction coefficient (approximate 0) of LiF layer.

First, we used FDTD simulations package in the Lumerical FDTD Solutions software (version 8.17.1072, 2017a) to perform the optical calculations and then to compute the TSC electrical characteristics. FDTD is a time domain method by using finite difference approximations to solve Maxwell's equations.[19,20,26,27] Except of neglecting diffraction and local electric field effects, it is more intuitive than other techniques and easier to get visual results which are good for designing and analyzing simulated structure.[28-30] We set corresponding parameters in FDTD as follows. The incident light plane wave was set to have a spectrum close to AM 1.5G (with λ between 300 and 1200 nm) and was oriented in the negative z-direction (see Figure 1 A). The thicknesses, refractive indexes, and extinction coefficients of different layers were set by adding corresponding structures and materials in FDTD. We obtained the normalized reflectance R (λ) and the transmittance T (λ) into c-Si using frequency-domain transmission monitors set on the top surface of the total solar cell and on the interface between ITO and silicon. We used the "power absorbed" (P_{abs}) analysis group in the FDTD package to get the absorptance of specific layers including the $PC_{60}BM$, perovskite, NiO, top ITO, and ITO layers by surrounding corresponding layers. Perfectly matched layer boundary conditions were used in the z-direction, and periodic boundary conditions were used in the x-y directions.

We then directly acquired the reflectance and the absorptance in top layers from the frequency-domain transmission monitor and the P_{abs} analysis group, respectively. The electron extraction was effective and sufficient because of appropriate work function resulting in forming an accumulation layer between ITO and $PC_{60}BM$,[31-33] so we assumed internal quantum efficiency of unity in the simulated materials. We can thus obtain the short-circuit current density (J_{sc}) by integrating the photon flux of the AM 1.5G solar spectrum with the corresponding absorptance. The J_{sc} was calculated using Equation (1):

$$J_{sc}^{(layer)} = \frac{q}{hc}\int \lambda E_{AM1.5G}(\lambda) P_{abs}^{(layer)}(\lambda) d\lambda, \quad (1)$$

where $E_{AM1.5G}(\lambda)$ is the incident photon energy flux and q is the electron charge.

We can calculate the J_{sc} of most layers including the $PC_{60}BM$, perovskite, NiO, top ITO, and ITO layers, but the J_{sc} of the silicon layer cannot be obtained in this way. This is because the difference in scale between the top and bottom cells (1 vs. 280 μm) makes the P_{abs} calculations in the silicon layer prohibitively memory intensive or even makes it not accomplishable. Shi et al[5] obtained the J_{sc} of silicon by subtracting the J_{sc} of the top layers from the full-spectrum current density calculated with an internal quantum efficiency of 1, but the simulated J_{sc} of silicon with this method is larger than that measured experimentally especially for λ > 1000 nm because of the ignorance of the rear surface reflection for long wavelengths. Gee et al[34] obtained the absorptance of silicon by assuming that the rays inside the silicon followed a random angular distribution. Nevertheless, a random angular distribution cannot be used to correctly describe the real light path here, as the incident light and reflected light paths are still fairly vertical.

Here, we proposed a hybrid method of FDTD with light path analysis to effectively simulate some special device structures, which cannot be directly treated by FDTD. Indeed, we used a frequency-domain transmission monitor (R_{ext}) positioned at the interface between ITO and silicon to get the light incident into silicon bottom cell. After absorbing by silicon, some of photons arrived in the silicon rear surface. Then, we used a frequency-domain transmission monitor positioned at the top of the silicon back surface (red dotted line shown in Figure 1A) to better understand the light path inside the silicon layer. By converting from vector coordinates to angles measured from the vector directions to the positive z-axis, we can get the angular distribution of the light reflected by the back surface of silicon. The 3-dimensional vector distribution for λ = 1100 nm along with the angular distribution is presented in Figure 1B. The reflected light with the angular distribution comes back toward the internal front surface of the silicon layer with a transmittance (T_θ) and a reflectance ($R_{int}(\theta,\theta')$). By iteratively summing the absorptance over the different possible reflection angles, we can calculate a more accurate absorptance value in the silicon layer. The absorptance of silicon is given as[34]

$$P_{abs}^{(Si)} = (1-R_{ext})\times[(1-T_0) + \sum_{\theta,\theta'}\left[T_0 R_{br}(\theta)(1-T_\theta) + T_0 T_\theta R_{br}(\theta) R_{int}\left(\theta,\theta'\right)(1-T_{\theta'}) + \cdots\right]], \quad (2)$$

where, as illustrated in Figure 1C, R_{ext} is the normalized reflectance at the initial interface, T_θ is the transmittance of an incident light at angle θ propagating from the top to the bottom surface of silicon layer, $R_{br}(\theta)$ is the normalized rear surface reflected angular distribution, and $R_{int}(\theta,\theta')$ is the normalized front surface reflected angular distribution for an incident light at angle θ. The incident light for λ < 1000 nm is rapidly absorbed and does not reach the rear surface, so the calculation is only valid for long wavelengths.

Next, we used the Shockley diode model to study overall performance of realistic perovskite/c-Si solar cell. This model has been used and verified in many papers[35-38] and can give correct relationships of electrical characteristics. The open-circuit voltage (V_{oc}) calculated from the J_{sc} by the Shockley diode equation is given as

$$V_{oc} = \frac{k_b T}{q} \ln\left(\frac{J_{sc}}{J_0} + 1\right), \quad (3)$$

where k_b is the Boltzman constant and T is the room temperature (298 K). J_0 is the diode saturation current density which can be obtained from experimental results: for different top perovskite cells, $J_0^{(Perovskite)}$ was derived from the current density-voltage curve of the perovskite solar cells acquired from recent literatures,[13,14,39,40] while $J_0^{(Si)} = 8.51 \times 10^{-12}$ mA/cm^2 was derived from the world record silicon heterojunction solar cell reported by Taguchi et al[41] with V_{oc} = 0.75 V and J_{sc} = 39.5 mA/cm^2. The fill factor (*FF*) was calculated using the well-established expression.[42]

$$FF = \frac{V_{oc} - \frac{k_b T}{q} \ln\left(\frac{qV_{oc}}{k_b T} + 0.72\right)}{V_{oc} + \frac{k_b T}{q}}. \quad (4)$$

The efficiency η of the simulated solar cell was obtained by

$$\eta = \frac{FF \times J_{sc} \times V_{oc}}{0.1 \mathrm{W/cm^2}} \quad (5)$$

Finally, we show in Figure 1D the plot of the simulated absorptance of both subcells in the monolithic TSCs, together with the measured EQE of both subcells.[14] We have already assumed that every absorbed photon generates a hole-electron pair, so the simulated absorptance is equal to the EQE. It is clear that the simulated absorptance is very close to experimental EQE especially at wavelengths ranging from 400 to 1200 nm. The main differences between the absorption and EQE curves are at wavelengths ranging from 800 to 1000 nm. One possible reason is from the thin amorphous silicon thin film layers (normally ~5 nm) being omitted in the simulation for simplification, which may increase the reflectance value. Secondly, it may be induced by the difference between the chosen thickness of silicon in the simulation and the real value in the experimental samples.[14] The proposed theoretical value may be lower than the real experimental thickness so that the simulated absorptance of silicon subcell is lower than the experimental EQE. By integrating the absorptance and EQE spectra over the AM 1.5G spectrum, we found that the simulated perovskite top cell and silicon bottom cell generated 18.9 and 18.1 mA/cm^2, respectively, which is very close to the measured results of 18.9 and 18.5 mA/cm^2. The differences between the absorptance and EQE yield less than 2% in the difference of J_{sc}, which is quite small for the simulation. The calculated cell's electric parameters (J_{sc} 18.1 mA/cm^2; V_{oc} 1.66 V; *Eff*. 23.7%) have little difference with realistic experimental parameters (J_{sc} 18.5 mA/cm^2; V_{oc} 1.62 V; *Eff*. 23.6%),[14] and can already prove the validity of the calculation method.[43] The reflection and parasitic absorption in the top ITO layer both play an important role in the current loss. Their optimization will be discussed in Section 5.

3 | PEROVSKITE/C-SI MONOLITHIC TSCS WITH VARYING PYRAMID SIZES IN REAR SURFACE

As a general principle, the geometry of the reflective rear surface determines the absorptance for long wavelengths in a silicon cell. Optimizing the pyramid-textured rear surface is thus a premise for achieving maximum efficiency in perovskite/c-Si TSCs. Baker-Finch et al[44] reported that the characteristic base angle α shown in Figure 1A of the pyramid texture was close to 50° to 52°. In addition, Shi et al[5] reported the relationship of reflectance at fixed period (*P*) or height (*H*), that was, *P* had an influence on the position of reflectance minimum, while *H* mainly influenced the magnitude of reflectance. We optimized the size (*P* and *H*) of pyramid-textured rear surface within that base angle α range after making a trade-off between the effects of *P* and *H*. Figures 1B and 2A to C show the angular distributions of the light reflected by the pyramid-textured rear surfaces in the perovskite/c-Si TSCs with 3 different pyramid sizes (for λ = 1100 nm): *P* = 5.0 μm and *H* = 3.0 μm in Figure 1B, planar in Figure 2A, *P* = 1.5 μm and *H* = 0.9 μm in Figure 2B, and *P* = 2.5 μm and *H* = 1.5 μm in Figure 2C, respectively. In comparison with a planar rear surface in Figure 2A, a pyramid-textured rear surface increases the average reflected angle, which increases absorptance, as the light path is longer. The average reflected angles of the 3 different sizes of pyramid-textured rear surfaces are 29° in Figure 2B, 45° in Figure 2C, and 43° in Figure 1B. Therefore, the best size to achieve highest average reflected angle is *P* = 2.5 μm and *H* = 1.5 μm. Figure 2D shows the reflectance of the perovskite/c-Si TSCs with a planar rear surface and the 3 different pyramid-textured rear surfaces. For λ = 1100 nm, the highest reflectance is 0.975, with the planar rear surface, and the lowest reflectance is 0.92, with *P* = 5.0 μm and *H* = 3.0 μm. It is obvious that a larger size leads to a lower reflectance. As a conclusion, we need to find the right trade-off between the reflectance and absorbed light path to get the maximum absorptance.

By using Equation (2), we calculated the absorptance of TSCs with different rear surface textures in Figure 2E. The J_{sc} calculated using Equation (1) from 1050 to 1200 nm are, respectively, 1.16 mA/cm^2 for planar, 2.14 mA/cm^2 for *P* = 1.5 μm and *H* = 0.9 μm, 2.30 mA/cm^2 for *P* = 2.5 μm and *H* = 1.5 μm, as well as 2.28 mA/cm^2 for *P* = 5 μm and *H* = 3 μm. Compared with the planar rear surface, the J_{sc} of the pyramid-textured rear surface with *P* = 2.5 μm and *H* = 1.5 μm can be increased by a factor of 2 from 1.16 to 2.30 mA/cm^2. The best geometric parameters were found to be *P* = 2.5 μm and *H* = 1.5 μm, different from those used in experiment with ca. *P* = 5.0 μm and *H* = 3.0 μm. That is, we can still optimize the size of pyramids of back surface in Bush et al[14] to get the best absorptance at long wavelengths.

To prove the veracity of our simulation, we further compared with the EQE results, reported by Werner et al,[13] of perovskite/c-Si TSCs on double-side-polished (DSP) and SST silicon bottom cells without antireflective layer. The detailed structures are as followed: ITO (150 nm)/Sprio-OMeTAD (150 nm)/perovskite ($MAPbI_3$, 300 nm)/$PC_{60}BM$ (20 nm)/ITO (30 nm)/silicon (300 μm)/ITO (100 nm)/Ag (150 nm) with a micron-sized (ca. *P* ~5 μm) pyramid-textured SST and a DSP rear surface. We show in Figure 2F the plot of the

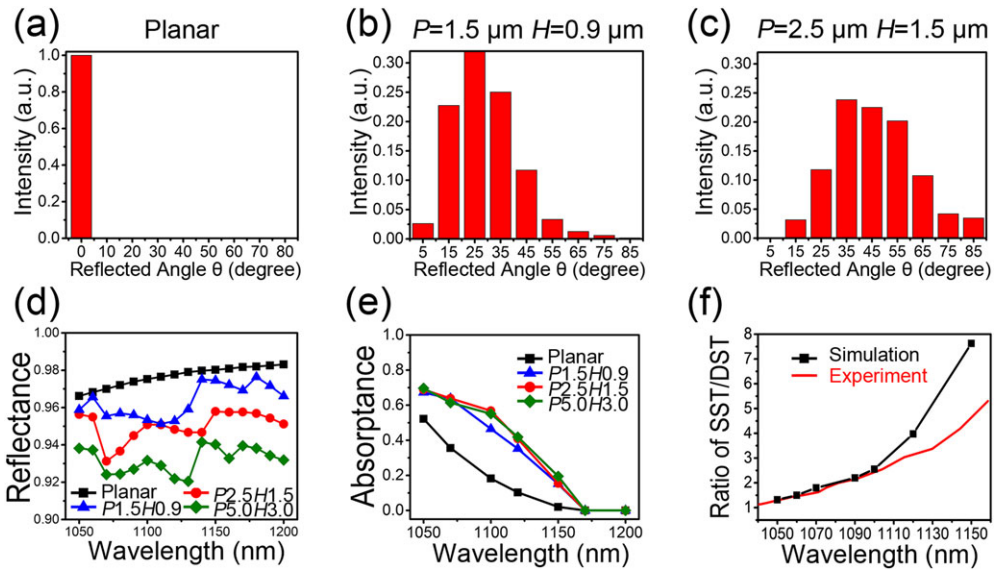

FIGURE 2 A-C, Angular distributions in the perovskite/c-Si monolithic TSCs with planar and 2 different pyramid sizes (for λ = 1100 nm): planar, P = 1.5 μm and H = 0.9 μm and P = 2.5 μm and H = 1.5 μm. D, E, Reflectance and absorptance of the perovskite/c-Si monolithic TSCs with planar and 3 different pyramid sizes (for wavelengths between 1050 and 1200 nm). F, Measured (red line) and the simulated (black line) absorptance ratio of SST and DSP TSCs [Colour figure can be viewed at wileyonlinelibrary.com]

measured absorptance ratio (red line) of SST and DSP TSCs, together with the simulated ratio (black line). For wavelengths between 1050 and 1120 nm, the simulated and measured ratios are extremely consistent. For wavelengths between 1120 and 1150 nm, the simulated ratio is higher than the measured ratio, which is because of the extinction coefficient of silicon in the bandgap (1.124 eV) being not accurate enough.

4 | PEROVSKITE/C-SI MONOLITHIC TSCS WITH VARYING BANDGAPS AND THICKNESSES OF PEROVSKITE LAYERS

In this section, to achieve the best matched short-circuit current density, we have simulated various perovskite/c-Si monolithic TSCs with 6 different bandgaps (E_g) of perovskite layers from 1.51 to 2.30 eV and 12 different perovskite layer thicknesses (d_p) from 200 to 750 nm. The thicknesses of the other layers were kept as in the previous section, as shown in Figure 1A. To calculate the absorption, we used the refractive indexes and extinction coefficients of perovskites with different bandgaps given in Ndione et al,24 and calculated the absorption curve using FDTD. The bandgaps were from perovskites of different compositions, and the samples were tested with reproducible experiments.[24] In short wavelength, the extinction coefficients remain almost unchanged for different bandgaps, while the extinction coefficients in long wavelength are negatively proportional with the bandgaps. We then calculated the $J_{sc}^{(Perovskite)}$ and the $J_{sc}^{(Si)}$ using Equation (1). The results presented in Figure 3A, B reveal that, in general, a larger d_p leads to a larger $J_{sc}^{(Perovskite)}$ in the top cell and a smaller $J_{sc}^{(Si)}$ in the bottom cell. Meanwhile, a larger E_g results in a smaller $J_{sc}^{(Perovskite)}$ in the top cell and a larger $J_{sc}^{(Si)}$ in the bottom cell. Therefore, there exists a region in which the $J_{sc}^{(Perovskite)}$ in the top cell can be equal to the $J_{sc}^{(Si)}$ in the bottom cell.

To further elucidate the light splitting mechanism, we have provided the wavelength dependence of the overall absorptance on the parameters d_p and E_g, respectively. Figure 3C, D shows the absorptance of perovskite and silicon layers for various E_gs (from 1.51 to 2.30 eV) at fixed d_p (450 nm). An increase in E_g results in a decrease in absorptance for a fixed wavelength. Therefore, the E_g determines the maximum absorptance of the perovskite layer at fixed d_p. When E_g is larger than 1.8 eV (700 nm), it is impossible to equalize $J_{sc}^{(Perovskite)}$ and $J_{sc}^{(Si)}$ by tuning d_p. Figure 3E, F illustrates the absorptance of the perovskite and silicon layers for different d_ps (from 200 to 500 nm) at fixed E_g (1.62 eV). Obviously, at wavelengths ranging from 300 to 500 nm, the absorptance of the perovskite layer is not dependent on d_p. This is because most of the light is absorbed by the top ITO layer and the perovskite layer. So, it does not reach the bottom of the perovskite layer. At wavelengths ranging from 500 to 700 nm, an increase in d_p leads to an increase in absorptance for the perovskite layer, which indicates that we can equalize $J_{sc}^{(Perovskite)}$ and $J_{sc}^{(Si)}$ by tuning d_p at fixed E_g. The dotted curves in Figure 3A, B represent the regions where $J_{sc}^{(Perovskite)}$ and $J_{sc}^{(Si)}$ are matched. Along these 2 curves, the common value of $J_{sc}^{(Perovskite)}$ and $J_{sc}^{(Si)}$ is equal to ca. 18.3 mA/cm^2, slightly larger than the experimental result of 18.1 mA/cm^2.[14]

5 | PEROVSKITE/C-SI MONOLITHIC TSCS WITH OPTIMIZING CURRENT LOSSES

In Section 4, we have achieved the best matched short-circuit current density by tuning perovskite layer thicknesses (d_p) and bandgaps (E_g). However, the cell surface reflection and parasitic absorption in the ITO layer still play an important role in the current loss. Therefore, we analyzed the current loss in different layers of the best-matched perovskite/c-Si TSCs discussed in Section 4. As shown in Figure 4A,

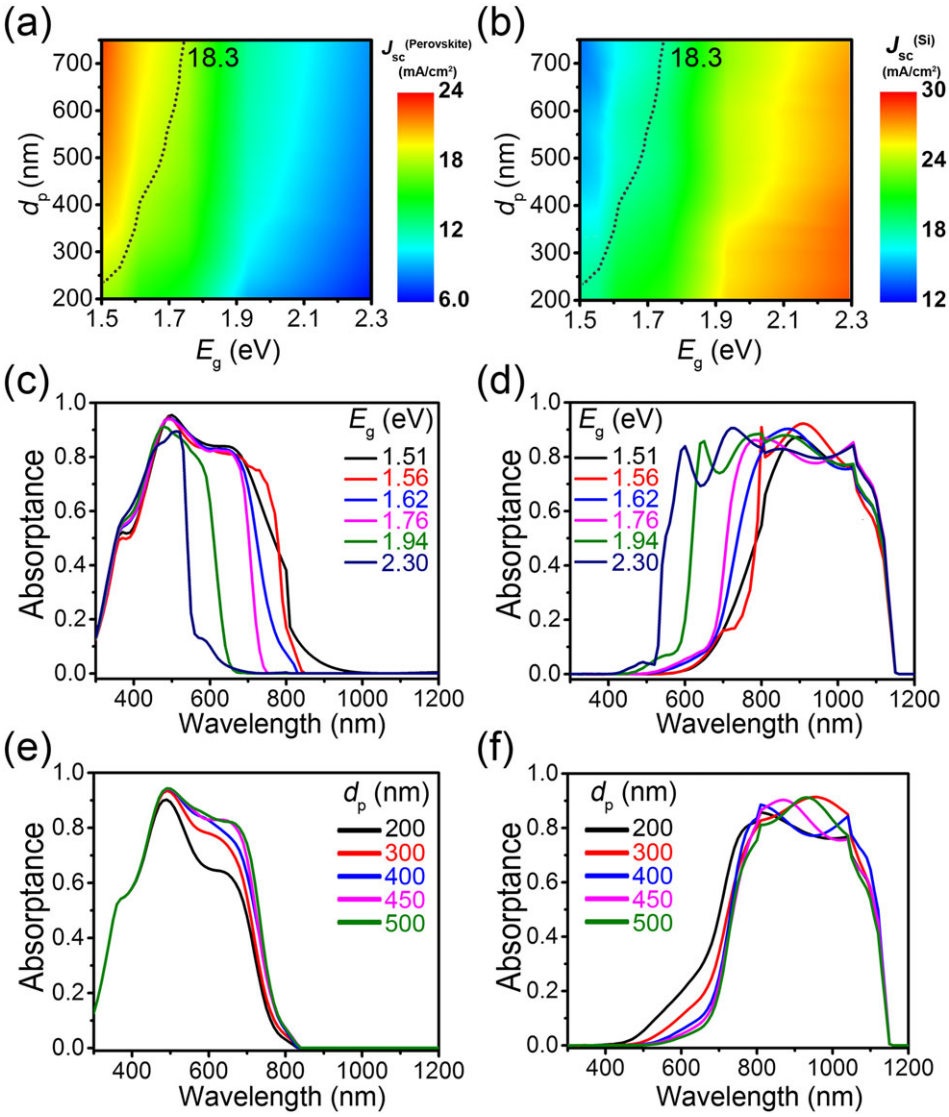

FIGURE 3 A, B, Contour of the short-circuit current density of perovskite layer ($J_{sc}^{(Perovskite)}$) and silicon layer ($J_{sc}^{(Si)}$) with different bandgaps (E_g) and thicknesses (d_p), respectively. The black dotted curves mark that the common value of $J_{sc}^{(Perovskite)}$ is equal to $J_{sc}^{(Si)}$. C, D, Absorptance of perovskite layer and silicon layer for various E_gs (from 1.51 to 2.30 eV) at fixed d_p (450 nm). E, F, Absoprtance of the perovskite and silicon layers for different d_ps (from 200 to 500 nm) at fixed E_g (1.62 eV) [Colour figure can be viewed at wileyonlinelibrary.com]

obviously, the cell surface reflection plays the most important roles in current loss and the minimum is ca. 6.9 mA/cm^2. The second loss comes from the parasitic absorption in the top ITO layer (ca. 2.1 mA/cm^2). Besides, the values of parasitic absorption in $PC_{60}BM$, NiO, and other layers are ca. 0.5, 0.2, and 0.1 mA/cm^2, respectively. These losses in surface reflection and top ITO layer will induce ca. 6% of efficiency drop compared to the whole, which can explain the limit of current experimental result as long as they keep flat in front surface. Therefore, optimizing the cell surface reflection and the parasitic absorption in the top ITO layer is the best way to enhance the efficiencies of the monolithic TSCs.

In general, the most effective way to improve reflection is to texture the front surface of bottom silicon solar cells,[45] because the thickness of top perovskite solar cell is too thin compared to the common size of pyramid texture. Therefore, we added a pyramidal front surface into our structure as shown in Figure 4C (the thicknesses and materials of others layers were kept identical to those in Figure 1A). We optimized the sizes of pyramid-textured front surface (period (P_{top})) and rear surface (period (P_{bottom})). The base angle α is within the base angle range discussed in Section 3. In Figure 4B, we show the short-circuit current loss caused by reflection ($J_{sc}^{(R)}$). The minimum is reached when P_{top} and P_{bottom} are equal to ~1 and ~2.5 μm, respectively, as marked by a dotted oval in Figure 4B. Compared with the value 6.9 mA/cm^2 of a structure with flat front surface as shown in Figure 4A, the minimum short-circuit current loss can be reduced to 2.9 mA/cm^2 in the optimized pyramid-textured front and rear surfaces of the best-matched perovskite/c-Si TSCs.

Holman et al[22] reported that the top ITO layer, which serves as an antireflection coating, should have a uniform thickness for a given structure. The thicknesses of top ITO layers are both 150 nm in articles reported by Werner et al[13] and Bush et al.[14] In addition, the absorptance of ITO is mainly determined by extinction coefficients which can be easily tuned by carrier density.[22,46] Therefore, we just optimized the current loss in the top ITO layer by tuning the carrier densities of the top ITO layer but not changing the thicknesses. The refractive indexes and extinction coefficients of different carrier

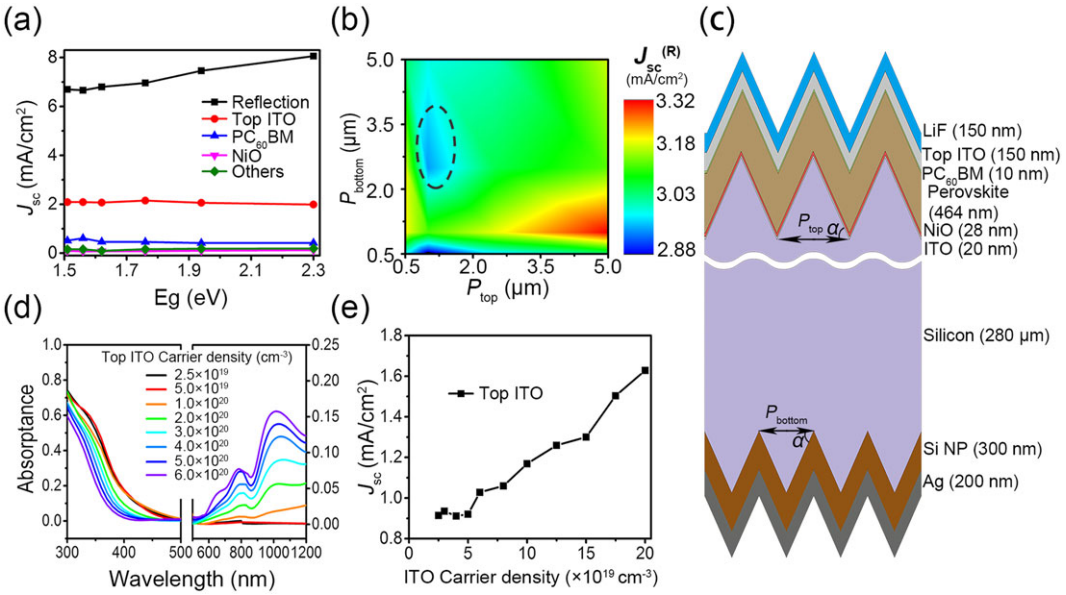

FIGURE 4 A, Current losses of the best current matched perovskite/c-Si monolithic TSCs with flat front surface. B, Contour of the short-circuit current density caused by reflection ($J_{sc}^{(R)}$) with different P_{top}s and P_{bottom}s. C, Schematic drawing of perovskite/c-Si monolithic TSCs with pyramid-textured front and pyramid-textured rear surfaces. The parameters α, P_{top}, and P_{bottom} denote the pyramid base angle and top and bottom pyramid periods, respectively. D, Absorptance of different top ITO layers with carrier densities ranging from 2.5×10^{19} to 6.0×10^{20} cm^{-3}. E, Current loss in top ITO layers with various carrier densities from 2.5×10^{19} to 2.0×10^{20} cm^{-3} [Colour figure can be viewed at wileyonlinelibrary.com]

densities of ITO materials were obtained from the recent literature.[22] Figure 4D shows the absorptance of different top ITO layers with carrier densities ranging from 2.5×10^{19} to 6.0×10^{20} cm^{-3}. We can easily conclude that, for wavelengths between 300 and 500 nm, a higher top ITO carrier density leads to a lower absorptance of the top ITO layer, but for wavelengths between 500 and 1200 nm, it is the opposite. We also can see that the absorptance at wavelengths between 300 and 500 nm is much higher than that at wavelengths between 500 and 1200 nm. Hence, there is a best top ITO carrier density for the lowest current loss in the top ITO layer. We calculated the current loss in different top ITO layers with various carrier densities from 2.5×10^{19} to 2.0×10^{20} cm^{-3} as shown in Figure 4E. The lowest current loss in the highest conductivity top ITO layer is ca. 0.9 mA/cm^2 with a corresponding carrier density of 5.0×10^{19} cm^{-3}. After this optimization, we can further increase short-circuit current density by 1.2 mA/cm^2 (absolute).

6 | DISCUSSION

In previous sections, we have optimized the size of pyramid-textured rear surface, the thickness (d_p) and bandgap (E_g) of the perovskite layer, the current losses in the top ITO layer, and the reflection, respectively. We have also calculated the electrical characteristics of the best current matched perovskite/c-Si monolithic TSCs as shown in Table 1.

On the upper part of Table 1, the monolithic TSCs, as shown in Figure 1A, have the following structure: flat front surface/LiF (150 nm)/top ITO (150 nm, with a carrier concentration of 2×10^{20} cm^{-3})/$PC_{60}BM$ (10 nm)/perovskite (material, E_g and d_p as seen in Table 1)/NiO (28 nm)/ITO (20 nm, with a carrier concentration of 5.0×10^{20} cm^{-3})/c-Si (280 μm)/silicon NP (300 nm)/Ag (200 nm)/pyramid-textured rear surface (P_{bottom} ~2.5 μm). The best efficiency is 25.28% when the material of the perovskite layer is $FA_{0.85}Cs_{0.15}Pb(Br_{0.4}I_{0.6})_3$ (E_g = 1.76 eV). Its absorption and reflection characteristics are shown in Figure 5A. The best-matched current J_{sc} is ca. 18.25 mA/cm^2. Besides, the current losses in the top ITO layer, $PC_{60}BM$, and reflection are ca. 2.13, 0.52, and 6.81 mA/cm^2, respectively. Compared with the experimental efficiency of 23.6%,[14] we can increase the efficiency by 1.68% (absolute) through optimizing the material of the perovskite layer. In addition, we can easily fabricate the corresponding devices by using the method reported by Bush et al[14] and only simply changing the material and thickness of the perovskite layer.

After addressing all the optimizations, on the lower part of Table 1 , the monolithic TSCs, as shown in Figure 4C, have the following structure: pyramid-textured front surface (P_{top} ~1 μm)/LiF (150 nm)/top ITO (150 nm, with a carrier concentration of 5×10^{19} cm^{-3})/$PC_{60}BM$

TABLE 1 Efficiencies and the corresponding parameters of the best current matched perovskite/c-Si monolithic TSCs with flat and pyramid-textured front surfaces

Texture	Material E_g (eV)	d_p (nm)	J_{sc} (mA/cm^2)	V_{oc} (V)	η (%)
Flat	$FA_{0.85}Cs_{0.15}PbI_3$ 1.51	236	18.25	1.53	21.13
	$MAPbI_3$ 1.56	272	18.26	1.75	24.28
	$FA_{0.85}Cs_{0.15}PbBrI_2$ 1.62	418	18.26	1.66	23.96
	$FA_{0.85}Cs_{0.15}Pb(Br_{0.4}I_{0.6})_3$ 1.76	778	18.25	1.82	25.28
Pyramid	$FA_{0.85}Cs_{0.15}PbI_3$ 1.51	240	20.51	1.53	24.44
	$MAPbI_3$ 1.56	290	20.47	1.76	27.96
	$FA_{0.85}Cs_{0.15}PbBrI_2$ 1.62	470	20.45	1.67	26.54
	$FA_{0.85}Cs_{0.15}Pb(Br_{0.4}I_{0.6})_3$ 1.76	820	20.44	1.83	29.05

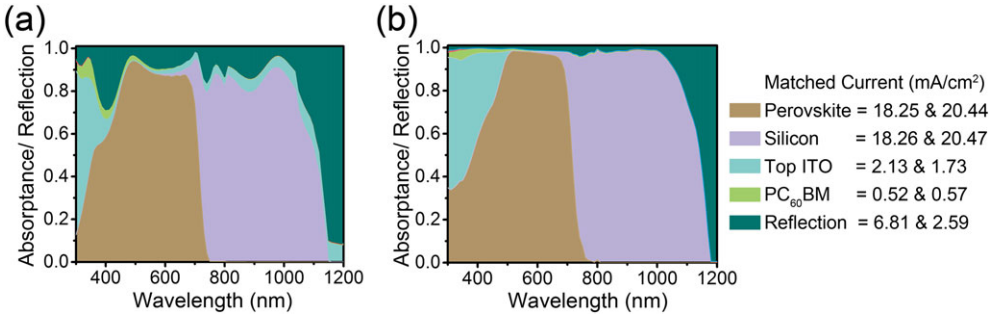

FIGURE 5 Simulated absorptance and reflectance of the best current matched perovskite/c-Si monolithic TSCs with (A) flat and (B) pyramid-textured front surfaces (perovskite material is $FA_{0.85}Cs_{0.15}Pb(Br_{0.4}I_{0.6})_3$), respectively [Colour figure can be viewed at wileyonlinelibrary.com]

(10 nm)/perovskite (material, E_g and d_p as seen in Table 1)/NiO (28 nm)/ITO (20 nm, with a carrier concentration of 5.0×10^{20} cm^{-3})/c-Si (280 μm)/silicon NP (300 nm)/Ag (200 nm)/pyramid-textured rear surface (P_{bottom} ~2.5 μm). Accordingly, the best efficiency is 29.05%, and the best-matched current J_{sc} is ca. 20.44 mA/cm^2. Its absorption and reflection characteristics are shown in Figure 5B. We can enhance the efficiency by 3.77% (absolute) compared with the best flat front surface result of 25.28%. In this case, the current losses in the top ITO layer, $PC_{60}BM$, and reflection are ca. 1.73, 0.57, and 2.59 mA/cm^2, respectively.

As for the preparation method,[14] the deposition methods of ITO, $PC_{60}BM$, and LiF, such as sputtering, pulsed chemical vapor deposition, and atomic layer deposition, can be easily transferred to the fabrication process of pyramid-textured perovskite/c-Si TSCs, as shown in Figure 4C. However, it is difficult to fabricate a uniform perovskite layer above a pyramid-textured front surface using traditional methods, such as 1-step precursor solution deposition,[47] 2-step sequential deposition,[48] and dual-source vapor deposition.[49] Therefore, we have to find a new method to achieve it. Fortunately, there may be some newly developed methods to achieve it, such as an electric field-assisted reactive deposition approach reported by Zhou et al[50] and a solvent-free deposition method reported by Chen et al.[51] Therefore, we can be confident that efficiencies above 29% can be achieved in perovskite/c-Si monolithic TSCs.

7 | CONCLUSIONS

In summary, we have introduced a composite method combining FDTD and light path analysis together for the tandem cell or devices. We have presented the optimized results of perovskite/c-Si monolithic TSCs with flat and pyramid-textured front surfaces from optical and electrical point of view by using this method. We have found an optimized set of pyramid parameters P_{bottom} ~2.5 μm in rear surface that enhances the absorption in long wavelengths (λ > 1000 nm). The best-matched short-circuit current density in a planar inverted structure is restricted by parasitic absorption in top ITO (ca. 2.1 mA/cm^2) and in cell surface reflection (ca. 6.8 mA/cm^2). By using the optimized carrier density of top ITO (5×10^{19} cm^{-3}) and sizes of pyramids in front surface of bottom silicon solar cells (P_{top} ~1 μm), the parasitic absorption in top ITO and in reflection is reduced to 1.7 and 2.5 mA/cm^2. Finally, the best-calculated efficiency of 29% is achieved at 1.76 eV perovskite bandgap and $FA_{0.85}Cs_{0.15}Pb(Br_{0.4}I_{0.6})_3$ perovskite material in monolithic configuration. These results will provide useful guidelines for the realization of high-efficient perovskite/c-Si monolithic TSCs.

ACKNOWLEDGEMENT

This work was supported by the Natural Science Foundation of China (11474201, 11674225, and 61234005).

ORCID

Lixiang Ba http://orcid.org/0000-0003-1118-0054

REFERENCES

1. Yoshikawa K, Kawasaki H, Yoshida W, Irie T, Konishi K, Nakano K, Uto T, Adachi D, Kanematsu M, Uzu H, Yamamoto K. Silicon heterojunction solar cell with interdigitated back contacts for a photoconversion efficiency over 26%. *Nature Energy*. 2017;2:17032-1-17032-8.*
2. Kojima A, Teshima K, Shirai Y, Miyasaka T. Organometal halide perovskites as visible-light sensitizers for photovoltaic cells. *J Am Chem Soc*. 2009;131(17):6050-6051.
3. NREL *Efficiency Chart* 2017. http://www.nrel.gov/ncpv/images/efficiency_chart.jpg. Accessed:2017-07.
4. Santbergen R, Mishima R, Meguro T, et al. Minimizing optical losses in monolithic perovskite/c-Si tandem solar cells with a flat top cell. *Opt Express*. 2016;24(18):A1288-A1299.
5. Shi D, Zeng Y, Shen W. Perovskite/c-Si tandem solar cell with inverted nanopyramids: Realizing high efficiency by controllable light trapping. *Sci Rep*. 2015;5:16504-1-16504-10.*
6. Jäger K, Korte L, Rech B, Albrecht S. Numerical optical optimization of monolithic planar perovskite-silicon tandem solar cells with regular and inverted device architectures. *Opt Express*. 2017;25(12):A473-A482.
7. Lunardi MM, Ho-Baillie AWY, Alvarez-Gaitan JP, Moore S, Corkish R. A life cycle assessment of perovskite/silicon tandem solar cells. *Prog Photovolt Res Appl*. 2017;25(8):679-695.
8. Albrecht S, Saliba M, Correa Baena JP, et al. Monolithic perovskite/silicon-heterojunction tandem solar cells processed at low temperature. *Energy Environ Sci*. 2016;9(1):81-88.
9. Chen B, Bai Y, Yu Z, Li T, Zheng X, Dong Q, Shen L, Boccard M, Gruverman A, Holman Z, Huang J. Efficient semitransparent perovskite solar cells for 23.0%-efficiency perovskite/silicon four-terminal tandem cells. *Adv Energy Mater*. 2016;6:1601128-1-1601128-7.*
10. Mcmeekin DP, Sadoughi G, Rehman W, et al. A mixed-cation lead mixed-halide perovskite absorber for tandem solar cells. *Science*. 2016;351(6269):151-155.

*Correction added on 28 June 2018, after first online publication: the issue and page details for these references have been corrected.

11. Peng J, Duong T, Zhou X, Shen H, Wu Y, Mulmudi H K, Wan Y, Zhong D, Li J, Tsuzuki T, Weber K J, Catchpole K R, White T P. Efficient indium-doped TiO_x electron transport layers for high-performance perovskite solar cells and perovskite-silicon tandems. *Adv Energy Mater*. 2017;7:1601768-1-1601768-10.*
12. Mailoa J P, Bailie C D, Johlin E C, Hoke E T, Akey A J, Nguyen W H, McGehee M D, Buonassisi T. A 2-terminal perovskite/silicon multijunction solar cell enabled by a silicon tunnel junction. *Appl Phys Lett*. 2015;106(12):121105-1-121105-4.*
13. Werner J, Barraud L, Walter A, et al. Efficient near-infrared-transparent perovskite solar cells enabling direct comparison of 4-terminal and monolithic perovskite/silicon tandem cells. *ACS Energy Lett*. 2016;1(2):474-480.
14. Bush K A, Palmstrom A F, Yu Z J, Boccard M, Cheacharoen R, Mailoa J P, McMeekin D P, Hoye R L Z, Bailie C D, Leijtens T, Peters I M, Minichetti M C, Rolston N, Prasanna R, Sofia S, Harwood D, Ma W, Moghadam F, Snaith H J, Buonassisi T, Holman Z C, Bent S F, McGehee M D. 23.6%-efficiency monolithic perovskite/silicon tandem solar cells with improved stability. *Nat Energy*. 2017;2:17009-1-17009-7.*
15. Matteocci F, Cinà L, Di Giacomo F, et al. High efficiency photovoltaic module based on mesoscopic organometal halide perovskite. *Prog Photovolt Res Appl*. 2016;24(4):436-455.
16. Dunbar RB, Moustafa W, Pascoe AR, et al. Device pre-conditioning and steady-state temperature dependence of $CH_3NH_3PbI_3$ perovskite solar cells. *Prog Photovolt Res Appl*. 2017;25(7):533-544.
17. Liu Z, Ren Z, Liu H, et al. A modeling framework for optimizing current density in four-terminal tandem cells: A case study on GaAs/Si tandem. *Sol Energy Mater Sol Cells*. 2017;170:167-177.
18. Liu Z, Ren Z, Liu H, Sahraei N, Lin F, Stangl R, Buonassisi T, Peters I M. Optical loss analysis of four-terminal GaAs/Si tandem solar cells. In: *43rd IEEE Photovoltaic Specialist Conference* 2016; Portland, USA.
19. Assadi MK, Hanaei H. Transparent carbon nanotubes (CNTS) as antireflection and self-cleaning solar cell coating. In: *Engineering Applications of Nanotechnology*. Springer International Publishing; 2017:101-114.
20. Kubota S, Kanomate K, Ahmmad B, Mizuno J, Hirose F. Optimized design of moth eye antireflection structure for organic photovoltaics. *J Coat Technol Res*. 2016;13(1):201-210.
21. Palik ED, Hunter WR. Lithium fluoride (LiF). In: *Handbook of optical constants of solids*. San Diego: Academic Press; 1985:675-693.
22. Holman Z C, Filipič M, Descoeudres A, De Wolf S, Smole F, Topič M, Ballif C. Infrared light management in high-efficiency silicon heterojunction and rear-passivated solar cells. *J Appl Phys*. 2013;113:013107-1-013107-13.*
23. Campoy-Quiles M, Müller C, Garriga M, Wang E, Inganäs O, Alonso MI. On the complex refractive index of polymer: Fullerene photovoltaic blends. *Thin Solid Films*. 2014;571:371-376.
24. Ndione PF, Li Z, Zhu K. Effects of alloying on the optical properties of organic–inorganic lead halide perovskite thin films. *J Mater Chem. C*. 2016;4(33):7775-7782.
25. Bakr NA, Salman SA, Shano AM. Effect of Co doping on structural and optical properties of NiO thin films prepared by chemical spray pyrolysis method. *Int Lett Chem Phys Astron*. 2014;41:15-30.
26. Garus S, Sochacki W. One dimensional photonic FDTD algorithm and transfer matrix method implementation for severin aperiodic multilayer. *J Appl Math Comput Mech*. 2017;16(4):17-27.
27. Le D-T, Nguyen M-C, Le T-T. Fast and slow light enhancement using cascaded microring resonators with sagnac reflector. *Optik-International Journal for Light and Electron Optics*. 2017;131:292-301.
28. Khan MA, Sichanugrist P, Kato S, Ishikawa Y. Theoretical investigation about the optical characterization of cone-shaped pin-Si nanowire for top cell application. *Energy Sci Eng*. 2017;4(6):383-393.
29. Jovanov V, Planchoke U, Magnus P, Stiebig H, Knipp D. Influence of back contact morphology on light trapping and plasmonic effects in microcrystalline silicon single junction and micromorph tandem solar cells. *Sol Energy Mater Sol Cells*. 2013;110:49-57.
30. Zhang C, Meier M, Hoffmann A, et al. Influence of interface textures on light management in thin-film silicon solar cells with intermediate reflector. *IEEE J Photovolt*. 2015;5(1):33-39.
31. Zhang J, Chen R, Wu Y, et al. Extrinsic movable ions in $MAPbI_3$ modulate energy band alignment in perovskite solar cells. *Adv Energy Mater*. 2018;8(5):1701981.
32. Zhou Y, Fuentes-Hernandez C, Shim J, et al. A universal method to produce low-work function electrodes for organic electronics. *Science*. 2012;336(6079):327-332.
33. Nie W, Tsai H, Asadpour R, et al. High-efficiency solution-processed perovskite solar cells with millimeter-scale grains. *Science*. 2015;347(6221):522-525.
34. Gee J M. The effect of parasitic absorption losses on light trapping in thin silicon solar cells. *Photovoltaic Specialists Conference, 1988; Conference Record of the Twentieth* IEEE 1988; 1: 549–554.
35. Obradovic A, Toch K, Coppens B, Khelifi S, Lauwaert J, Thybaut K. Non-isothermal modeling of dark current-voltage measurements of a CIGS solar cell. *ECS J Solid State Sci Technol*. 2018;7(2):50-54.
36. Shuttle CG, Hamilton R, O'Regan BC, Nelson J, Durrant JR. Charge-density-based analysis of the current-voltage response of polythiophene/fullerene photovoltaic devices. *Proc Natl Acad Sci USA*. 2010;107(38):16448-16452.
37. Dawidowski W, Sciana B, Lindert IZ, et al. The influence of top electrode of InGaAsN/GaAS solar cell on their electrical parameters extracted from illuminated I-V characteristics. *Solid-State Electron*. 2016;120:13-18.
38. Strandberg R. Analytic J V-characteristics of ideal intermediate band solar cells and solar cells with up and downconverters. *IEEE Trans Electron Devices*. 2017;64(5):2275-2282.
39. Pang S, Hu H, Zhang J, et al. $NH_2CH{=}NH_2PbI_3$: An alternative organolead iodide perovskite sensitizer for mesoscopic solar cells. *Chem Mater*. 2014;26(3):1485-1491.
40. Wang Z, Lin Q, Chmiel F P, Sakai N, Herz L M, Snaith H J. Efficient ambient-air-stable solar cells with 2D-3D heterostructured butylammonium-caesium-formamidinium lead halide perovskites. *Nat Energy*. 2017;2:17135-1-17135-10.*
41. Taguchi M, Yano A, Tohoda S, et al. 24.7% record efficiency HIT solar cell on thin silicon wafer. *IEEE J Photovolt*. 2014;4(1):96-99.
42. Green MA. Accuracy of analytical expressions for solar cell fill factors. *Solar Cells*. 1982;7(3):337-340.
43. Sun X, Asadpour R, Nie W, Mohite AD, Alam MA. A physics-based analytical model for perovskite solar cells. *IEEE J Photovolt*. 2015;5(5):1389-1394.
44. Baker-Finch SC, McIntosh KR. Reflection distributions of textured monocrystalline silicon: Implications for silicon solar cells. *Prog Photovolt Res Appl*. 2013;21(5):960-971.
45. Zhong S, Wang W, Tan M, Zhuang Y, Shen W. Realization of quasi-omnidirectional solar cells with superior electrical performance by all-solution-processed Si nanopyramids. *Adv Sci*. 2017;1700200-1-1700200-9.*
46. Zhao L, Zhou C, Li H, Diao H, Wang W. Design optimization of bifacial HIT solar cells on p-type silicon substrates by simulation. *Sol Energy Mater Sol Cells*. 2008;92(6):673-681.
47. Kim HS, Lee CR, Im JH, et al. Lead iodide perovskite sensitized all-solid-state submicron thin film mesoscopic solar cell with efficiency exceeding 9. *Sci Rep*. 2012;2(591):1-7.
48. Burschka J, Pellet N, Moon SJ, et al. Sequential deposition as a route to high-performance perovskite-sensitized solar cells. *Nature*. 2013;499(7458):316-319.

*Correction added on 28 June 2018, after first online publication: the issue and page details for these references have been corrected.

49. Liu M, Johnston MB, Snaith HJ. Efficient planar heterojunction perovskite solar cells by vapour deposition. *Nature*. 2013;501(7467):395-398.

50. Zhou F, Liu H, Wang X, Shen W. Fast and controllable electric-field-assisted reactive deposited stable and annealing-free perovskite toward applicable high-performance solar cells. *Adv Funct Mater*. 2017;27:1606156-1-1606156-14.*

51. Chen H, Ye F, Tang W, et al. A solvent- and vacuum-free route to large-area perovskite films for efficient solar modules. *Nature*. 2017;550(7674):92-1-92-4.*

How to cite this article: Ba L, Liu H, Shen W. Perovskite/c-Si tandem solar cells with realistic inverted architecture: Achieving high efficiency by optical optimization. *Prog Photovolt Res Appl*. 2018;1–10. https://doi.org/10.1002/pip.3037

*Correction added on 28 June 2018, after first online publication: the issue and page details for these references have been corrected.